Atmos. Meas. Tech. Discuss., 7, 11303–11343, 2014
www.atmos-meas-tech-discuss.net/7/11303/2014/
doi:10.5194/amtd-7-11303-2014

Atmospheric Measurement Techniques Discussions

Impact of meteorological clouds on satellite detection and retrieval of volcanic ash during the Eyjafjallajökull 2010 and Grímsvötn 2011 eruptions: a modelling study

A. Kylling[1], N. Kristiansen[1], A. Stohl[1], R. Buras-Schnell[2], C. Emde[3], and J. Gasteiger[3]

[1]NILU – Norwegian Institute for Air Research, P.O. Box 100, 2027 Kjeller, Norway
[2]Schnell algorithms, Am Erdäpfelgarten 1, 82205 Gilching, Germany
[3]Meteorological Institute, Ludwig-Maximilians-University, Munich, Germany

Received: 22 August 2014 – Accepted: 27 October 2014 – Published: 18 November 2014

Correspondence to: A. Kylling (arve.kylling@nilu.no)

Published by Copernicus Publications on behalf of the European Geosciences Union.

Abstract

Volcanic ash is commonly observed by infrared detectors on board Earth orbiting satellites. In the presence of ice and/or liquid water clouds the detected volcanic ash signature may be altered. In this paper the effect of ice and liquid water clouds on detection and retrieval of volcanic ash is quantified by simulating synthetic equivalents to satellite infrared images with a 3-D radiative transfer model. The simulations were made both with and without realistic water and ice clouds taken from European Centre for Medium-Range Weather Forecast (ECMWF) analysis data. The volcanic ash cloud fields were taken from simulations by the Lagrangian particle dispersion model FLEXPART. The radiative transfer calculations were made for the geometry and channels of the Spinning Enhanced Visible and Infrared Imager (SEVIRI), for the full duration of the Eyjafjallajökull 2010 and Grímsvötn 2011 eruptions. The synthetic SEVIRI images were then used as input to standard reverse absorption ash detection and retrieval methods. Meteorological clouds were on average found to reduce the number of detected ash affected pixels by 6–12 %. However, the effect was highly variable and for individual scenes up to 40 % of pixels with mass loading $> 0.2\,\mathrm{g\,m^{-2}}$ could not be detected due to the presence of water and ice clouds. The detection efficiency (detected ash pixels relative to Flexpart ash pixels with ash loading $> 0.2\,\mathrm{g\,m^{-2}}$) was on average only 14.6 % (22.1 %) for the cloudy (cloudless) simulation for the Eyjafjallajökull 2010 eruption, and 3.6 % (10.0 %) for the Grímsvötn 2011 eruption. If only Flexpart ash pixels with ash loading $> 1.0\,\mathrm{g\,m^{-2}}$ are considered the detection efficiency increase to 54.7 % (74.7) for the Eyjafjallajökull 2010 eruption and to 4.8 % (15.1 %) for the Grímsvötn 2011 eruption. For coincident pixels, i.e., pixels where ash was both present in the Flexpart simulation and detected by the algorithm, the presence of meteorological clouds overall increased the retrieved mean mass loading for the Eyjafjallajökull 2010 eruption by about 13 %, while for the Grímsvötn 2011 eruption ash mass loadings the effect was a 4 % decrease of the retrieved ash mass loading. However, larger differences were seen between scenes (SD of ±30 and ±20 % for Eyjafjallajökull and Grímsvötn re-

AMTD
7, 11303–11343, 2014

spectively) and even larger ones within scenes. If all pixels are included the total mass from all scenes is severely underestimated. For the Eyjafjallajökull 2010 eruption the cloudless (cloudy) mass is underestimateed by 52 % (66 %) compared to the Flexpart mass, while for the Grímsvötn 2011 eruption the Flexpart mass is underestimated by 82 % (91 %) for the cloudless (cloudy) simulation. The impact of ice and liquid water clouds on the detection and retrieval of volcanic ash, implies that to fully appreciate the location and amount of ash, satellite ash measurements should be combined with ash dispersion modelling.

1 Introduction

Volcanic ash clouds can have a number of impacts on the environment and society, including alteration of the radiative balance of the atmosphere and the Earth's climate (Robock, 2000; Timmreck, 2012), and disruption to aviation (Casadevall, 1994). Infrared (IR) detectors in space are key tools for tracking and monitoring ash clouds. Commonly used ash detection methods are variations of the reverse absorption method (e.g. Prata, 1989; Francis et al., 2012; Prata and Prata, 2012). This method explores the brightness temperature difference ($\Delta T = T_{10.8} - T_{12.0}$) between the 10.8 ($T_{10.8}$) and 12.0 ($T_{12.0}$) µm regions of the thermal infrared spectrum. For volcanic ash $\Delta T < 0$ while $\Delta T \geq 0$ for liquid water and ice clouds. This method was, for example, successfully used on data from the Spinning Enhanced Visible and Infrared Imager (SEVIRI) on board the Meteosat Second Generation (MSG, Meteosat-9) geostationary satellite, for the Eyjafjallajökull 2010 eruption (Stohl et al., 2011; Prata and Prata, 2012). After detection of ash affected pixels, various methods (Wen and Rose, 1994; Francis et al., 2012; Prata and Prata, 2012) may be used to retrieve mass loading and effective radius of the ash cloud. Several factors influence the infrared detection and retrieval of volcanic ash, including ash cloud density and altitude (temperature), ash particle composition, shape and size distribution, the atmospheric temperature profile, humidity, and the surface temperature (Wen and Rose, 1994; Corradini et al., 2008;

AMTD
7, 11303–11343, 2014

Kylling et al., 2014). In addition, the presence of ice and/or liquid water clouds may change ΔT and affect the detection of ash and the retrieval of ash cloud properties. In retrievals, assumptions are typically made about the composition, shape and size distribution of the ash particles. Ash cloud temperature and surface temperature may either be retrieved or taken from weather forecast models. Finally, the presence of ice and/or liquid water clouds is usually not considered.

The aim of this paper is to investigate the effect of ice and liquid water clouds on detection and retrieval of volcanic ash. To do so cases with volcanic ash in the presence of ice and/or liquid water clouds must be compared with very similar cases but without ice and liquid water clouds. Such an investigation can not readily be made based on experimental methods due to the inherent problem in distinguishing cloudy and cloudless cases. Furthermore, ice and liquid water cloud information together with volcanic ash cloud information is needed for such an investigation, but this information is difficult to obtain. To overcome this problem, a model-based approach is adopted. Images equivalent to the SEVIRI 10.8 and 12.0 µm channels were simulated with a 3-D radiative transfer model, for the full duration of the Eyjafjallajökull 2010 and Grímsvötn 2011 eruptions. Simulations were made both with and without realistic water and ice clouds taken from European Centre for Medium-Range Weather Forecast (ECMWF) analyses. The volcanic ash cloud fields were taken from simulations by the Lagrangian particle dispersion model Flexpart. These synthetic images were used as input to ash detection and retrieval methods.

Simulated satellite scenes have been used by several authors to evaluate algorithms for detection of liquid water and ice cloud properties. For example Bugliaro et al. (2011) simulated a SEVIRI scene over Germany, with cloud input from the COSMO-EU weather model, to compare and validate cloud retrievals. Jonkheid et al. (2012) developed a fast SEVIRI simulator to quantify cloud water path retrieval uncertainties using the Regional Atmospheric Climate Model. Wind et al. (2013) calculated synthetic MODerate resolution Imaging Spectroradiometer (MODIS) radiances using cloud information from the Goddard Earth Observing System Version 5 (GEOS-5) Earth system

AMTD
7, 11303–11343, 2014

model. They used the simulated radiances as input to standard MODIS retrievals and compared these with retrievals using real MODIS data and were able to locate and quantify problems with GEOS-5 cloud optical properties and cloud vertical distributions.

During development of satellite detection and retrieval algorithms the outcomes of these algorithms must be compared and tested against "true value" data sets. These data sets may come from either observations or simulations of the property of interest. By simulated properties we understand properties retrieved from simulated satellite images, whereas observed properties are retrieved from measured images. Model properties are input to the radiative transfer model that generated the simulated satellite images. Several routes are possible in the comparison of different atmospheric property data sets. Jonkheid et al. (2012) have summarized these routes in their Fig. 1: Route I: compare observed properties with model properties; Route II: compare observed and simulated radiances; Route III: compare model properties with simulated properties; and Route IV: compare observed properties with simulated properties. Here we use Route III to quantitatively estimate the effects of liquid water and ice clouds on detection and retrieval of volcanic ash. For single scenes qualitative comparisons are made following route IV.

The remainder of the paper is organised as follows: in Sect. 2 the simulation of the IR images is described together with the input data. The ash detection and retrieval methods are described in Sect. 3. The results are presented in Sect. 4 and impacts of ice and liquid water clouds on detection and retrieval of volcanic ash clouds are discussed in Sect. 5.

2 Simulation of infrared SEVIRI images

The simulation of infrared SEVIRI images has been described in detail by Kylling et al. (2013) and will only be briefly summarized here. The radiative transfer is calculated by the 3-D Monte Carlo code for the physically correct tracing of photons in cloudy atmo-

AMTD
7, 11303–11343, 2014

spheres (MYSTIC) (Mayer et al., 2010; Emde et al., 2010; Buras and Mayer, 2011), which gets ash cloud fields input from the Lagrangian particle dispersion model Flexpart (Stohl et al., 1998, 2005) and ice and liquid water clouds from European Centre for Medium-Range Weather Forecast (ECMWF) analysis. While Kylling et al. (2013) used the LOWTRAN gas absorption parameterization (Pierluissi and Peng, 1985; Ricchiazzi et al., 1998) we here adopt the recent, more accurate and faster REPTRAN parameterization of Gasteiger et al. (2014).

Stohl et al. (2011) used Flexpart to calculate the 3-D dispersion of ash from the Eyjafallajökull 2010 eruption using optimized emissions based on inverse modelling with SEVIRI and IASI (Infrared Atmospheric Sounding Interferometer) measurements. The ash concentrations were calculated with a horizontal resolution of $0.25^\circ \times 0.25^\circ$ and a vertical resolution of 250 m for 25 particle size classes with radii in the range 0.125–125 µm (see Stohl et al. (2011) for details). Examples of the total ash column from the Flexpart model simulations are shown in the top left panels of Figs. 1 and 2.

These two cases are shown as they demonstrate two different effects of ice and liquid water clouds in volcanic ash observations, as will be discussed in more detail below. Only pixels with column density above $0.2\,\mathrm{g\,m^{-2}}$ are shown. This limit was chosen as it corresponds to the low contamination limit of $0.2\,\mathrm{mg\,m^{-3}}$ for an ash cloud of 1 km vertical thickness defined in connection with the Eyjafjallajökull eruption (International Air Carrier Association (IACA), 2010). For the Grímsvötn 2011 eruption the 3-D ash clouds estimated by Moxnes et al. (2014) using Flexpart combined with optimized emissions based on inversion modelling with IASI measurements, were used as input to the radiative transfer simulations.

The ice and liquid water clouds were taken from ECMWF analysis data with horizontal resolution of $0.25^\circ \times 0.25^\circ$ and 91 vertical model levels. The 2-D ECMWF ice and liquid water fields for the level closest to the FLEXPART output layer was interpolated to the FLEXPART output resolution as described by Kylling et al. (2013). ECMWF data are available every six hours. Consequently, radiative transfer simulations were performed for 00:00, 06:00, 12:00 and 18:00 UTC each day of the eruptions (14 April–24 May

AMTD
7, 11303–11343, 2014

2010, for Eyjafallajökull; 21–27 April 2011, for Grímsvötn). Examples of total columns of the liquid water and ice water cloud profiles are shown in the top centre and right plots, respectively, of Figs. 1 and 2. Surface and atmospheric temperatures were also taken from ECMWF analysis.

The ash, ice and liquid water cloud fields given in latitude/longitude coordinates were horizontally re-gridded to a 200 × 320 rectangular grid required by MYSTIC with a resolution of about 28 km × 16 km. The vertical resolution was as for the Flexpart simulation (i.e., 250 m). For each grid cell the ash, ice and liquid water cloud optical properties were calculated as described by Kylling et al. (2013). The radiative transfer calculations were made by the MYSTIC 3-D model, which was run within the libRadtran model framework (Mayer and Kylling, 2005). While MYSTIC can handle 3-D clouds the libRadtran/MYSTIC framework does not allow 3-D fields of trace gases. Hence a constant water vapour profile from the subarctic summer atmosphere from Anderson et al. (1986) was adopted over the whole domain. Brightness temperatures were calculated for the 10.8 and 12.0 µm channels and the viewing geometry of SEVIRI. Cloudy images with ash, ice and liquid water clouds were calculated in addition to cloudless images containing only ash (see lower left and centre plots of Figs. 1 and 2 for examples). A total of 184 (Eyjafjallajökull: 159; Grímsvötn: 25) images were calculated for each channel (2) for cloudy and cloudless conditions. This totals to 736 simulated images, each taking about 2 h of CPU hours using 10 nodes on a Linux cluster. The standard deviation of the simulated brightness temperature was less than 0.25 K for more than 94 % of the pixels. This is of similar magnitude as the requirements for the noise equivalent delta temperature (NEΔT)[1] of 0.25 and 0.37 K for the 10.8 and 12.0 µm SEVIRI channels and slightly larger than the actual NEΔT performance of 0.11 and 0.15 K, respectively (Schmetz et al., 2002).

[1] "The noise equivalent delta temperature is the amount of incident signal temperature that would be needed to match the internal noise of the detector such that the signal-to-noise ratio is equal to one". (From http://en.wikipedia.org/wiki/Noise-equivalent_temperature.)

AMTD
7, 11303–11343, 2014

3 Ash detection and retrieval

The reverse absorption technique was used to identify pixels affected by ash (Prata, 1989). A conservative cut-off temperature difference, $\Delta T_{\text{cut}} = -0.5$ K, was used to avoid too many false positives. This means that pixels with $\Delta T < \Delta T_{\text{cut}}$ were identified as containing ash. It is noted that water vapour absorption decrease the magnitude of ΔT and may be corrected for (Yu et al., 2002). No water vapour correction was applied in the analysis presented here. At large viewing angles the SEVIRI pixel size increases significantly, see Fig. 1 of Prata and Prata (2012), thus data were required to have a viewing angle smaller than 70°.

A spatial noise reduction technique was applied to remove isolated patches of pixels detected as ash. For each detection of an ash affected pixel, the surrounding pixels north, south, and to the east and west, were also required to be identified as ash, otherwise the pixel was rejected. This is a slightly stronger requirement than the spatial noise reduction applied by Francis et al. (2012). They required that a least 6 out of 9 pixels in a 3 × 3 surrounding block were ash-flagged for the center pixel to be retained. The spatial noise reduction was only applied to the measured SEVIRI data and not to the simulated data due to larger pixel sizes.

If the optical depth ($\tau_{10.8}$) and effective radius (r_{e}) of the ash cloud are known, the ash mass loading m_{l} for each pixel can be calculated (Wen and Rose, 1994)

$$m_{\text{l}} = \frac{4}{3}\rho \frac{\tau r_{\text{e}}}{Q_{\text{ext}}(r_{\text{e}})}. \quad (1)$$

In Eq. (1) it is assumed that the ash composition and hence the extinction efficiency (Q_{ext}) and density (ρ) are known, and that the size distribution within each pixel is uniform (mono-disperse).

The ash cloud optical depth and effective radius were retrieved using a modification of the Bayesian optimal estimation technique described by Francis et al. (2012). They used the SEVIRI 10.8, 12.0 and 13.4 µm brightness temperatures to retrieve the

AMTD
7, 11303–11343, 2014

ash layer pressure, the ash column mass loading and the ash size distribution effective radius. Prata and Prata (2012) derived the ash cloud optical depth and the ash size distribution effective radius from the SEVIRI 10.8 and 12.0 µm brightness temperatures using a look-up-table based approach. In this study we use the SEVIRI 10.8 and 12.0 µm brightness temperatures to retrieve the independent ash cloud optical depth, $\tau_{10.8}$ and the ash size distribution effective radius by minimizing the cost function (Francis et al., 2012)

$$J(\boldsymbol{x}) = (\boldsymbol{x} - \boldsymbol{x}^b)^{\mathrm{T}}\mathbf{B}^{-1}(\boldsymbol{x} - \boldsymbol{x}^b) + (\boldsymbol{y}^{\mathrm{ob}} - \boldsymbol{y}(\boldsymbol{x}))^{\mathrm{T}}\mathbf{R}^{-1}(\boldsymbol{y}^{\mathrm{ob}} - \boldsymbol{y}(\boldsymbol{x})). \quad (2)$$

where the atmospheric state vector $\boldsymbol{x} = (\tau_{10.8}, r_{\mathrm{e}})$, the prior atmospheric state vector $\boldsymbol{x}^b = (0.5, 3.5)$, and $\mathbf{B}$ is the error covariance matrix of the a priori background. The error covariance matrix $\mathbf{B}$ was assumed to be diagonal and the variances of the state variables were set to $\sigma^2_{\tau_{10.8}} = (10)^2$ and $\sigma^2_{r_{\mathrm{e}}} = (10\,\mu\mathrm{m})^2$ (Francis et al., 2012). The values in $\mathbf{B}$ are large compared to the desired retrieval accuracy, thus the background state only provides a weak constraint. The observations are the brightness temperatures at 10.8 and 12.0 µm, $\boldsymbol{y}^{\mathrm{ob}} = (T_{10.8}, T_{12.0})$, while $\boldsymbol{y}(\boldsymbol{x})$ are the brightness temperatures for the state vector $\boldsymbol{x}$ as calculated by the libRadtran radiative transfer model (Mayer and Kylling, 2005). For the forward calculations of $\boldsymbol{y}(\boldsymbol{x})$ the ash cloud was assumed to be vertically homogeneous and 1 km thick in the vertical. The measurement error covariance matrix is denoted by $\mathbf{R}$. The values for $\mathbf{R}$ were taken from Table 1 of Francis et al. (2012) who assumed $\mathbf{R}$ to be diagonal with $R_{11} = (1.11\,\mathrm{K})^2$ and $R_{22} = (1.11\,\mathrm{K})^2$. For the forward calculations the ash particles were assumed to be spherical and have a log-normal size distribution. The geometric standard deviation of the size distribution was 1.5.

The $T_{10.8}$ and $T_{12.0}$ brightness temperatures also depend on the surface temperature and the ash cloud temperature. These may either be retrieved by including information from more channels (Francis et al., 2012); obtained from weather forecasting models; or estimated from for example the 12.0 µm image (Prata and Prata, 2012). Here the

AMTD
7, 11303–11343, 2014

latter approach is chosen. For a given pixel the surface (ash cloud) temperature is taken to be the maximum (minimum) temperature of a block of 29 × 29 surrounding pixels centred on the pixel.

4 Results

The effect of ice and liquid water clouds on ash detection and retrieval is illustrated below for two selected SEVIRI scenes during the Eyjafjallajökull 2010 eruption. Further quantitative evaluations for the whole eruption periods of the Eyjafjallajökull 2010 and Grímsvötn 2011 eruptions are given in Sects. 4.1 and 4.2, respectively.

The effect of ice and liquid water clouds on the simulated 10.8 µm brightness temperatures can be seen in Figs. 1 and 2. In the cloudless simulations (lower left plots) the ash cloud is clearly visible by comparison to the locations of Flexpart modelled ash cloud. Other variability in the cloudless $T_{10.8}$ simulations is caused by variations in surface emissivity and surface temperature, for example over Greenland, the Alps and the mountain ranges of Norway. Including ice and liquid water clouds in the image simulations changes $T_{10.8}$ dramatically (lower centre). The 10.8 µm brightness temperatures as measured by SEVIRI for the same time as the simulated images, are shown in the lower right plots of Figs. 1 and 2. There are clear similarities between the cloudy simulated and measured images. Common features coupled to the addition of ice and liquid water clouds are clearly visible; for example the cloud systems over Iceland and Sweden in Fig. 1, and over the East coast of Greenland and Northern Spain in Fig. 2. The ash cloud is seen in both simulated and measured images, at least in areas with sufficient high ash mass loadings and homogeneous cloud fields. However, numerous differences between the simulated cloudy and measured images discussed by Kylling et al. (2013), are evident, for example the too warm brightness temperatures in the North Sea in the simulations. These differences are attributed to uncertainties in representation of cloud and temperature fields and the coarser spatial resolution in the simulations.

AMTD
7, 11303–11343, 2014

The ash detection technique as described previously in Sect. 3, was applied to the cloudless and cloudy simulated images, as well as to the measured data. This provides an evaluation of the impact of ice and water clouds on the ash detection. Figures 3 and 4 show examples of the ash detection on the simulated and measured data from Figs. 1 and 2. The pixels with Flexpart ash columns above the low contamination limit ($0.2\,g\,m^{-2}$) are compared with the pixels flagged as ash by the reverse absorption technique in the cloudless simulation (left) and cloudy simulation (centre) of Figs. 3 and 4. The Flexpart columns with ash columns above the low contamination limit are given as the union of blue and green pixels. The green pixels are termed coincident pixels and are those with Flexpart column above the low contamination limit and identified as containing ash using the ash detection method described previously in Sect. 3. The blue coloured pixels are false negatives, i.e. prescribed as ash from the Flexpart simulations, but detection by the simulated image/detection framework failed. The red pixels are identified as ash but they contain no ash according to the Flexpart simulations, consequently they are false positives. The $\Delta T = T_{10.8} - T_{12.0} < -0.5\,K$ brightness temperature differences calculated from SEVIRI measurements for the same situations are shown in the right plots of Figs. 3 and 4. For the Eyjafjallajökull 2010 and Grímsvötn 2011 eruptions time series of data similar to those in Figs. 3 and 4 were generated. These data and Figs. 3 and 4 are further discussed in Sects. 4.1 and 4.2 below.

The next step is to apply the ash retrieval technique as described previously in Sect. 3, to the cloudless and cloudy simulated images, as well as to the measured data. This allows an evaluation of the impact of meteorological clouds on the ash retrieval. Examples of retrieved ash mass loading for the simulated scenes in Figs. 1 and 2 are shown in Figs. 5 and 6, respectively, while the ash mass loading retrieved from the measured SEVIRI data are shown in Fig. 7. The retrieved ash mass loadings based on the cloudless simulated images (left plots) are in good agreement with the Flexpart ash distribution (Figs. 1 and 2). Including meteorological clouds causes both over- and under-estimates of the ash mass loading compared to the cloudless situation (middle and right plots).

AMTD
7, 11303–11343, 2014

By comparing the SEVIRI simulated cloudless and cloudy retrievals in Figs. 5 and 6 with the SEVIRI measured retrievals in Fig. 7 it is tempting to conclude that the cloudy simulations better represent the measurements, at least for the 15 April when the ice and liquid water clouds have a larger effect (cf. left and middle plot of Fig. 3). However, a direct comparison between the SEVIRI simulated ash retrieval and the SEVIRI measured ash retrieval is non-trivial as the simulated data have a coarser spatial resolution compared to the measured SEVIRI data. A thorough and complete comparison of the SEVIRI simulated ash retrieval and the SEVIRI measured ash retrieval for the Eyjafjallajökull 2010 and Grímsvötn 2011 eruptions is beyond the scope of this work.

To further evaluate the effect of meteorological clouds on volcanic ash retrieval, data corresponding to Figs. 5 and 6 were calculated for all simulated scenes of the Eyjafjallajökull 2010 and Grímsvötn 2011 eruptions.

4.1 Eyjafjallajökull 2010

All simulated and measured satellite scenes for the total duration of the Eyjafjallajökull 2010 eruption period (14 April–20 May) were analysed to quantify the effect of meteorological clouds. Time series for coincidence and false positive ash detections (as in Figs. 3 and 4), as well as retrieved total ash mass loadings (as in Figs. 5 and 6), were generated from all simulated scenes. Figure 8 shows the time series for the ash detection analysis. The percentage of pixels in a scene with Flexpart ash above the low contamination limit is shown by the blue line. The percentage of coincidences, i.e. Flexpart ash pixels identified as ash by the reverse absorption technique, is shown by the green lines. The solid (dashed) green line pertains to simulations with (without) ice and liquid water clouds. The red lines are the percentages of false positives, that is pixels that are identified as ash by the reverse absorption technique, but do not contain ash according to the Flexpart data (Flexpart column smaller than $0.2\,\mathrm{g\,m^{-2}}$). The number of false negatives, that is pixels that do contain ash but are not detected, are shown in black. The solid (dashed) black and green lines adds up to the blue line. A number of interesting features are present in Fig. 8:

AMTD
7, 11303–11343, 2014

– far fewer pixels are identified as ash than are present in the Flexpart simulated ash fields (used as input to the detection method).

– Clouds have a variable impact on the number of pixels identified as ash (compare solid and dashed green lines).

– The number of false positives exhibits a diurnal variation. The diurnal variation is larger for the cloudless simulations.

For the whole eruption period only 14.6 % (22.1 %) of the pixels with ash above the low contamination limit (0.2 g m^{-2}) are identified as ash for the cloudy (cloudless) simulation. If a limit of 1.0 g m^{-2} is used the number of pixels identified as ash increases to 54.7 % (74.7 %) for the cloudy (cloudless) simulation. There appears to be no strong dependence in the ash detection on the satellite viewing angle as demonstrated by the green lines in Fig. 9. For satellite viewing angles smaller than 51° the detection efficiency is high (compare blue and green lines in Fig. 9). The number of false positives increases strongly with increasing viewing angle (red lines in Fig. 9), indicating that at large viewing angles ash detection is less reliable. Interestingly the number of false positives is larger for the cloudless than for the cloudy simulations. The cloudless false positives are mostly found over land (Scandinavia) and are larger at night than at day. This is caused by strong atmospheric temperature inversions near the surface when the surface cools more strongly than the overlying atmosphere during nighttime (Platt and Prata, 1993). In April the ECMWF surface temperatures over Scandinavia exhibited comparatively large diurnal variations. These variations declined in magnitude at the end of April and into May, as seen by the smaller number of false positives towards the end of the period shown. The presence of clouds obscures the surface and consequently reduces the diurnal variation for those pixels affected by clouds. The pixels not affected by clouds will still have diurnal variation. Hence, the number of false positives is generally reduced with the presence of clouds (compare solid and dashed red lines in Fig. 8). As stated in Sect. 2 the water vapour profile used in the radiative transfer

AMTD
7, 11303–11343, 2014

calculations, is constant over the domain. This may give a too humid atmosphere at certain locations and as a result, further increases the number of false positives.

To further understand why far fewer pixels are identified as ash than are present in the Flexpart simulated ash fields, the frequency of false negatives relative to the number of Flexpart pixels is calculated and shown in Fig. 10 as a function of ash cloud mass loading and altitude. It is seen that most ash pixels that miss detection either have a mass loading less than 0.5 g m^{-2} or are below 3 km altitude. There are also ash pixels missing detection around 10 km. These are associated with increased emissions of ash on 15 May (Stohl et al., 2011). There are also pixels missed around 5 km altitude for mass loadings larger than 5 g m^{-2}. The ash cloud may be missed due to either overlying or overlapping meteorological clouds or too small temperature difference with the underlying surface, where the radiatively effective surface under the ash cloud is the Earth's surface or an opaque liquid water cloud. The mostly small difference between the number of false negatives between cloudless and cloud simulations (black lines in Fig. 8) indicates that for the situation during the Eyjafjallajökull 2010 eruption, the small temperature difference between the Earth's surface and the ash cloud due to the low altitude of the ash cloud, was the main reason for the rather large number of false negatives.

The presence of meteorological clouds tends to obscure ash clouds compared to cloudless skies (compare solid and dashed green lines in Fig. 8). The effect of meteorological clouds varies as the overlap with the ash cloud changes. The mean of the number of pixels detected as ash relative to Flexpart ash pixels for each scene in the cloudy simulations was fairly constant between the first (14–21 April) and second (5–21 May) eruption periods, being 13.0 % ± 9 % and 15.6 % ± 14.8 % respectively. For the cloudless simulations these numbers are 25.2 % ± 17.0 % and 21.4 % ± 16.0 %, indicating that the presence of clouds reduced ash detection more in the first period (by 12.2 %) than in the second period (5.8 %). The large standard deviations indicate large variability between scenes. Upon inspection of individual scenes it is found that clouds may obscure up to 40 % of the Flexpart pixels identified as ash. It is noted that for some

AMTD
7, 11303–11343, 2014

cases (8 May) more pixels are identified as ash for the cloudy than for the cloudless simulation. No or small cloud effects are present on days 15 April and 6–8 May.

Further, the presence of meteorological clouds on the total ash mass retrieval for the whole Eyjafjallajökull 2010 eruption period was assessed. The total ash cloud mass for each scene was calculated from ash mass loading retrievals for cloudless and cloudy simulated SEVIRI scenes of which examples are shown in Figs. 5 and 6. Time series of the ash mass loading for pixels detected as ash and with Flexpart ash columns above the low contamination limit are shown in the upper plot of Fig. 11. Notice that only coincident pixels (i.e., Flexpart ash present and also detected) were used for these calculations. The presence of meteorological clouds mainly gives a larger ash mass loading estimate compared to a cloudless sky except for 7–8 May, as seen in the lower plot of Fig. 11. For the whole eruption the cloudless (cloudy) simulation underestimates the Flexpart mass by about 38 % (25 %). However, as noted above, for individual scenes clouds cause both over- and underestimates, see right panels in Figs. 5 and 6. The ash mass retrieved depends on the surface temperature. For the present retrieval this was deduced from $T_{12.0}$, see Sect. 3. In the presence of meteorological clouds $T_{12.0}$ will be lower compared to a cloudless sky. Also, the brightness temperature difference will be smaller for the cloudy scene. Both these factors interact to cause both over- and underestimates of the ash mass loading.

Above only coincident pixels were included. If all pixels, also false positives, are included it is found that for the whole eruption the cloudless (cloudy) simulation underestimates the Flexpart mass by about 52 % (66 %). For both the cloudless and cloudy simulations this mass difference is mostly due to Flexpart ash pixels that are not detected. As more Flexpart ash pixels are missed for the cloudy simulations the mass underestimate is larger for the cloudy simulations compared to the cloudless simulations.

AMTD
7, 11303–11343, 2014

4.2 Grímsvötn 2011

The impact of meteorological clouds on ash detection and retrieval is further analysed for the whole duration of the Grímsvötn eruption, 21–27 May 2011. The modelled and retrieved ash mass loadings for the whole period are shown as mosaics in Fig. 12. The upper left plot illustrates the transport of ash as modelled by Flexpart at six hourly (00:00, 06:00, 12:00, 18:00 UTC) intervals. The periodic pattern is due to the six hourly sampling. The upper right (lower right) plot shows the ash mass loading retrieved from the simulated cloudy (cloudless) SEVIRI images. The lower left panel shows ash mass loading retrieved from SEVIRI measurements for the same 6 hourly intervals. During the start of the eruption the ash (and SO_2) was transported northwards. A strong signal is seen in the measured SEVIRI image (lower left). Note that the mass loadings presented here for the northwards plume are about a factor 2 larger than those derived from IASI measurements and presented by Moxnes et al. (2014). SEVIRI also tracks the south-easterly movement of the ash cloud for the later phases of the eruption. This compares well with the IASI data presented by Moxnes et al. (2014) in their Fig. 2. To fully understand the reasons for the difference between SEVIRI and IASI in the northwards plume and the agreement in the south-east plume requires detailed comparison of the SEVIRI and IASI retrieval, which is beyond the scope of this study.

It is noted that the emissions used for the Flexpart estimated ash fields for the Grímsvötn 2011 eruption were based on IASI data (Moxnes et al., 2014), while for the Eyjafjallajökull 2010 eruption they were based on both IASI and SEVIRI data (Stohl et al., 2011). This implies that the comparisons of the simulated and measured SEVIRI images to the Flexpart model simulation are fully independent only for the Grímsvötn case.

The cloudy simulation (upper right panel in Fig. 12) shows no ash south and south-east of Iceland as is seen in the Flexpart and measured SEVIRI images. Some of this ash is present in the cloudless simulations (lower right plot, Fig. 12), but far less than in the Flexpart simulation. Figure 13 further illustrates the number of pixels that

AMTD
7, 11303–11343, 2014

are identified as ash by the detection algorithm. The number of Flexpart pixels with ash mass loading above the contamination limit is shown by the blue line, while the percentage of ash pixels identified as ash for the cloudy and cloudless simulations are shown as solid and dashed green lines, respectively. For the eruption 3.6 % (10 %) of the ash pixels above the low contamination limit are detected for the cloudy (cloudless) simulation. If a limit of 1.0 g m^{-2} is used the number of pixels identified as ash increases to 4.8 % (15.1 %) for the cloudy (cloudless) simulation.

The dependence of Flexpart ash pixels and detected and false positives pixels on viewing angle is presented in Fig. 14. As for the Eyjafjallajökull 2010 eruption, Fig. 9, the number of false positives increases strongly with viewing angle and is larger for the cloudless than the cloudy simulation. The frequency of false negatives as a function of ash mass loading and ash cloud altitude is given in Fig. 15. The pattern is similiar to the Eyjafjallajökull 2010 eruption. Most ash pixels that miss detection are either at altitudes lower than 4 km or have a mass loading less than 0.5 g m^{-2}. Some ash pixels are also missed around 10 km. These are associated with the northwards travelling plume at the start of the eruption.

The total ash cloud mass for coincident pixels is shown in Fig. 16. Only data up to 24 April is shown as for the cloudy simulation ash is detected only for the first few days of the eruption, see Figs. 12 and 13. For the coincident pixels in Fig. 16 the cloudless (cloudy) mass overestimates the Flexpart mass by 28 % (24 %). This is opposite to the underestimation we found in Sect. 4.1 for the Eyjafjallajökull 2010 eruption. However, for shorter time periods, 14–16 May, overestimates were also present for the Eyjafjallajökull 2010 eruption Fig. 11.

For the whole eruption the cloudless (cloudy) simulation underestimates the Flexpart mass by about 82 % (91 %) if all pixels (also false positives) are included. This mass difference is mostly due to the large fraction of Flexpart ash pixels that remain undetected.

AMTD
7, 11303–11343, 2014

5 Discussion

The detection of ash affected pixels depends on the difference between the surface temperature and the ash cloud temperature. The effective ash emissions were generally at higher (about 6 km) altitudes for Eyjafjallajökull compared to Grímsvötn (2–3 km, except for 22 May), see Fig. 2 in Stohl et al. (2011) and Fig. 3 in Moxnes et al. (2014), respectively. The overall lower altitude of the Grímsvötn ash explains why relatively less of it was detected in the simulations presented in Sect. 4, due to smaller temperature differences between the ash cloud and the surface and more mixing with low altitude meteorological clouds.

For the Grímsvötn 2011 eruption ash was detected over Scandinavia by both SEVIRI, see lower left plot in Fig. 12, and IASI (see Fig. 2 in Moxnes et al., 2014). The lack of detected ash in the cloudy simulated scenes (upper right plot in Fig. 12), and the presence in the cloudless simulated scenes, lower right plot Fig. 12, indicate that the liquid water and ice clouds used in the cloudy simulations did not well represent the real cloud situations. This may be due to the clouds being misplaced in altitude and/or horizontal position such as to obscure the Flexpart ash cloud.

As described in Sect. 2 a constant water vapour profile was used over the whole domain. For a single scene on 11 May 2010 for the Eyjafjallajökull 2010 eruption Kylling et al. (2013) estimated that the fixed water vapour profile on average increased the 10.8–12.0 µm brightness temperature difference by 0.07 K for pixels identified as ash. As a result, for the single scene they investigated, about 8 % of ash affected pixels missed detection by assuming a fixed water vapour profile. Consequently, the overall detection efficiency would increase by including a spatially varying water vapour profile. Since we are mostly interested in the difference in ash detection and retrieval between the cloudless and cloudy simulated scenes, which are similarly affected by the assumption of a constant water vapour profile, it is not anticipated that a constant water vapour profile will affect the results presented.

AMTD
7, 11303–11343, 2014

The ash mass loadings retrieved from the simulated images for coincident pixels are generally lower than the Flexpart ash mass loadings for the Eyjafjallajökull 2010 eruption, see Fig. 11. For the whole eruption period the Flexpart mean ash mass for coincident pixels was 1.75×10^8 kg. This compares to 1.09×10^8 and 1.32×10^8 kg for the cloudless and cloudy simulations. The opposite occurred for the Grímsvötn 2011 eruption; the Flexpart mean ash for coincident pixels was 7.19×10^6 kg while it was higher for the cloudless (9.17×10^6 kg) and cloudy (8.90×10^6 kg) simulations. However, the standard deviations are large being 30 and 20 % for Eyjafjallajökull and Grímsvötn respectively. Hence, the cloud impact varies considerably between scenes. Furthermore, inspection of the right plot of Figs. 5 and 6 reveals both under- and overestimates of the mass loading due to the presence of clouds within a single scene. For individual pixels the difference may be larger than 100 %.

For coincident pixels both over- and underestimations of the mass loading happens. If all pixels are included the total mass from all scenes is severely underestimated. For the Eyjafjallajökull 2010 eruption the cloudless (cloudy) mass is underestimateed by 52 % (66 %) compared to the Flexpart mass, while for the Grímsvötn 2011 eruption the Flexpart mass is underestimated by 82 % (91 %) for the cloudless (cloudy) simulation. This is mainly caused by the low ash detection efficiency, which is due to the low altitudes of the ash clouds during most of the Eyjafjallajökull 2010 and Grímsvötn 2011 eruptions.

Clouds do affect the brightness temperatures and hence the retrieval of ash mass. For cloudless scenes one might expect that the simulated cloudless mass loading retrievals should agree with the mass loading from the Flexpart model. However, although the ash type, density and particle shape are the same in the retrieval and the Flexpart simulations there are also differences. Particularly, the retrieval method assumes a log-normal particle size distribution (see Sect. 3), which is different from the size distribution of the Flexpart simulated ash particles. Indeed, the Flexpart size distribution is different for each voxel making up the ash cloud field. It is also noted that according to Kristiansen et al. (2012) Flexpart may have too little mass for particles with radii in

AMTD
7, 11303–11343, 2014

the 0.5–5 µm range. This is the size range where the retrieval method discussed here is most sensitive. The ash cloud thickness is also different in the Flexpart simulations and in the retrieval where a fixed 1 km thick ash layer is assumed.

6 Conclusions

For the Eyjafjallajökull 2010 and Grímsvötn 2011 eruptions ash cloud fields from the Lagrangian particle dispersion model Flexpart have been input to the MYSTIC 3-D radiative transfer model to simulate SEVIRI-like 10.8 and 12.0 µm brightness temperatures with and without the presence of liquid water and ice clouds. Images of brightness temperatures were simulated at six hourly intervals limited by the temporal resolution of the liquid water and ice clouds fields from ECMWF. Ash affected pixels were detected in the images based on the reverse absorption technique. Furthermore, optimal estimation was used to retrieve ash mass loading. Comparisons of the detected and retrieved ash from images with and without liquid water and ice clouds showed that:

- the detection efficiency (detected ash pixels relative to Flexpart ash pixels with ash loading $> 0.2\,\mathrm{g\,m^{-2}}$) was on average 14.6 % (22.1 %) for the cloudy (cloudless) simulation for the Eyjafjallajökull 2010 eruption, and 3.6 % (10.0 %) for the Grímsvötn 2011 eruption. These numbers increased to 54.7 % (74.7) for the Eyjafjallajökull 2010 eruption and to 4.8 % (15.1 %) for the Grímsvötn 2011 eruption if only Flexpart ash pixels with ash loading $> 1.0\,\mathrm{g\,m^{-2}}$ were considered.

- The mostly small difference between the number of false negatives between cloudless and cloudy simulations (black lines in Figs. 8 and 13) indicates that for the situation during the eruptions, the small temperature difference between the Earth's surface and the ash cloud was the main reason for the rather large number of false negatives. The small temperature difference was due to the low altitude of the ash cloud.

AMTD
7, 11303–11343, 2014

- The presence of meteorological clouds mostly led to identification of fewer ash affected pixels (Figs. 8 and 13). On average during the full duration of the eruptions ice and liquid water clouds were found to decrease the number of detected ash pixels by about 6–12 %. However, variations were large between scenes and clouds reduced ash detection by up to 40 % for individual scenes. Dispersed and thinned ash clouds were most likely to go undetected. For a few cases more ash pixels were identified in the presence of meteorological clouds.
- Diurnal variations were seen in the number of false positives. These mostly occurred over cloudless land areas and were caused by large diurnal variations in surface temperatures while the atmospheric temperature remained comparatively constant (nighttime temperature inversions).
- The number of false positives increased with increasing viewing angle and care should be used for data with viewing angles larger than about 69°.
- The presence of ice and liquid water clouds gave both smaller (4 % Grímsvötn) and larger (13 % Eyjafjallajökull) mean ash mass loading compared to the cloudless situation for coincident pixels, i.e., pixels where ash was both present in the Flexpart simulation and detected by the algorithm. However, large differences were seen between scenes (standard deviation of ±30 and ±20 % for Eyjafjallajökull and Grímsvötn respectively) and even larger within scenes.
- If all pixels are included the total mass from all scenes is severely underestimated. For the Eyjafjallajökull 2010 eruption the cloudless (cloudy) mass is underestimateed by 52 % (66 %) compared to the Flexpart mass, while for the Grímsvötn 2011 eruption the Flexpart mass is underestimated by 82 % (91 %) for the cloudless (cloudy) simulation. This is due to the low detection efficiency.

The results suggest that a two-layer retrieval (ash cloud overlying liquid water cloud) is needed to further improve ash mass loading estimates under cloudy conditions (Grainger et al., 2013). Also, detection methods that explore the temporal behaviour

AMTD
7, 11303–11343, 2014

of ash clouds between consecutive satellite images may prove fruitful (see for example Naeger and Christopher, 2014). The ultimate goal may be the direct assimilation of satellite-observed radiances in a weather forecast model that also emits and transports ash.

Ice and liquid water clouds interfere with the detection and retrieval of volcanic ash. During a volcanic ash situation, the measurements from satellite instruments should be combined with inverse ash dispersion modelling (Stohl et al., 2011) to get a as complete as possible picture of where and how much ash is present.

The present analyses pertain to the situation during the Eyjafjallajökull 2010 and Grímsvötn 2011 eruptions. For other eruptions taking place under other meteorological situations and with other eruption heights the impact of meteorological clouds may be different.

Acknowledgements. This work received support from the FP7 project FUTUREVOLC "A European volcanological supersite in Iceland: a monitoring system and network for the future", (grant agreement no: 308377), the Norwegian Research Council (Contract 224716/E10) and the Norwegian Ministry of Transport and Communications. EUMETSAT are acknowledged for providing SEVIRI data via EUMETCast.

References

Anderson, G., Clough, S., Kneizys, F., Chetwynd, J., and Shettle, E.: AFGL atmospheric constituent profiles (0–120 km), Tech. Rep. AFGL-TR-86-0110, Air Force Geophys. Lab., Hanscom Air Force Base, Bedford, Mass., 1986. 11309

Bugliaro, L., Zinner, T., Keil, C., Mayer, B., Hollmann, R., Reuter, M., and Thomas, W.: Validation of cloud property retrievals with simulated satellite radiances: a case study for SEVIRI, Atmos. Chem. Phys., 11, 5603–5624, doi:10.5194/acp-11-5603-2011, 2011. 11306

Buras, R. and Mayer, B.: Efficient unbiased variance reduction techniques for Monte Carlo simulations of radiative transfer in cloudy atmospheres: the solution, J. Quant. Spectrosc. Ra., 112, 434–447, doi:10.1016/j.jqsrt.2010.10.005, 2011. 11308

AMTD
7, 11303–11343, 2014

Casadevall, T. J.: The 1989–1990 eruption of Redoubt Volcano, Alaska, impacts on aircraft operations, J. Volcanol. Geoth. Res., 62, 301–316, 1994. 11305

Corradini, S., Spinette, C., Carboni, E., Tirelli, C., Buongiorno, M. F., Pugnaghi, S., and Gangale, G.: Mt. Etna tropospheric ash retrieval and sensitivity analysis using Moderate Resolution Imaging Spectroradiometer Measurements, J. Appl. Remote Sens., 2, 023550, doi:10.1117/1.3046674, 2008. 11305

Emde, C., Buras, R., Mayer, B., and Blumthaler, M.: The impact of aerosols on polarized sky radiance: model development, validation, and applications, Atmos. Chem. Phys., 10, 383–396, doi:10.5194/acp-10-383-2010, 2010. 11308

Francis, P. N., Cooke, M. C., and Saunders, R. W.: Retrieval of physical properties of volcanic ash using Meteosat: a case study from the 2010 Eyjafjallajökull eruption, J. Geophys. Res., 117, D00U09, doi:10.1029/2011JD016788, 2012. 11305, 11310, 11311

Gasteiger, J., Emde, C., Mayer, B., Buras, R., Buehler, S., and Lemke, O.: Representative wavelengths absorption parameterization applied to satellite channels and spectral bands, J. Quant. Spectrosc. Ra., 148, 99–115, doi:10.1016/j.jqsrt.2014.06.024, 2014. 11308

Grainger, R. G., Peters, D. M., Thomas, G. E., Smith, A. J. A., Siddans, R., Carboni, E., and Dudhia, A.: Measuring volcanic plume and ash properties from space, Geol. Soc. Spec. Publ., 380, 293–320, doi:10.1144/SP380.7, 2013. 11323

International Air Carrier Association (IACA): Volcanic Ash – flying into areas of known or forecasted volcanic ash contamination, available at: http://www.iaca.be/php/issues/index.php?doc_id=3688 (last access: 13 November 2014), 2010.

Jonkheid, B. J., Roebeling, R. A., and van Meijgaard, E.: A fast SEVIRI simulator for quantifying retrieval uncertainties in the CM SAF cloud physical property algorithm, Atmos. Chem. Phys., 12, 10957–10969, doi:10.5194/acp-12-10957-2012, 2012. 11306, 11307

Kristiansen, N. I., Stohl, A., Prata, A. J., Bukowiecki, N., Dacre, H., Eckhardt, S., Henne, S., Hort, M. C., Johnson, B. T., Marenco, F., Neininger, B., Reitebuch, O., Seibert, P., Thomson, D. J., Webster, H. N., and Weinzierl, B.: Performance assessment of volcanic ash transport model mini-ensemble used for inverse modeling of the 2010 Eyjafjallajökull eruption, J. Geophys. Res., 117, D00U11, doi:10.1029/2011JD016844, 2012. 11321

Kylling, A., Buras, R., Eckhardt, S., Emde, C., Mayer, B., and Stohl, A.: Simulation of SEVIRI infrared channels: a case study from the Eyjafjallajökull April/May 2010 eruption, Atmos. Meas. Tech., 6, 649–660, doi:10.5194/amt-6-649-2013, 2013. 11307, 11308, 11309, 11312, 11320

AMTD
7, 11303–11343, 2014

Kylling, A., Kahnert, M., Lindqvist, H., and Nousiainen, T.: Volcanic ash infrared signature: porous non-spherical ash particle shapes compared to homogeneous spherical ash particles, Atmos. Meas. Tech., 7, 919–929, doi:10.5194/amt-7-919-2014, 2014. 11306

Mayer, B. and Kylling, A.: Technical note: The libRadtran software package for radiative transfer calculations – description and examples of use, Atmos. Chem. Phys., 5, 1855–1877, doi:10.5194/acp-5-1855-2005, 2005. 11309, 11311

Mayer, B., Hoch, S. W., and Whiteman, C. D.: Validating the MYSTIC three-dimensional radiative transfer model with observations from the complex topography of Arizona's Meteor Crater, Atmos. Chem. Phys., 10, 8685–8696, doi:10.5194/acp-10-8685-2010, 2010. 11308

Moxnes, E. D., Kristiansen, N. I., Stohl, A., Clarisse, L., Durant, A., Weber, K., and Vogel, A.: Separation of ash and sulfur dioxide during the 2011 Grímsvötn eruption, J. Geophys. Res.-Atmos., 119, 7477–7501, doi:10.1002/2013JD021129, 2014. 11308, 11318, 11320

Naeger, A. R. and Christopher, S. A.: The identification and tracking of volcanic ash using the Meteosat Second Generation (MSG) Spinning Enhanced Visible and Infrared Imager (SEVIRI), Atmos. Meas. Tech., 7, 581–597, doi:10.5194/amt-7-581-2014, 2014. 11324

Pierluissi, J. H. and Peng, G.-S.: New molecular transmission band models for LOWTRAN, Opt. Eng., 24, 541–547, 1985. 11308

Platt, C. M. R. and Prata, A. J.: Nocturnal effects in the retrieval of land surface temperatures from satellite measurements, Remote Sens. Environ., 45, 127–136, 1993. 11315

Prata, A. J.: Infrared radiative transfer calculations for volcanic ash clouds, Geophys. Res. Lett., 16, 1293–1296, 1989. 11305, 11310

Prata, A. J. and Prata, A. T.: Eyjafjallajökull volcanic ash concentrations determined using Spin Enhanced Visible and Infrared Imager measurements, J. Geophys. Res., 117, D00U23, doi:10.1029/2011JD016800, 2012. 11305, 11310, 11311

Ricchiazzi, P., Yang, S., Gautier, C., and Sowle, D.: SBDART: A research and teaching software tool for plane-parallel radiative transfer in the Earth's atmosphere, B. Am. Meteorol. Soc., 79, 2101–2114, 1998. 11308

Robock, A.: Volcanic eruptions and climate, Rev. Geophys., 138, 191–219, 2000. 11305

Schmetz, J., Pili, P., Tjemkes, S., Just, D., Kerkmann, J., Rota, S., and Ratier, A.: Supplement to an introduction to Meteosat Second Generation (MSG), radiometric performance of SEVIRI, B. Am. Meteorol. Soc., 83, 991–991, doi:10.1175/BAMS-83-7-Schmetz-1, 2002. 11309

AMTD
7, 11303–11343, 2014

Stohl, A., Hittenberger, M., and Wotawa, G.: Validation of the Lagrangian particle dispersion model FLEXPART against large scale tracer experiment data, Atmos. Environ., 32, 4245–4264, 1998. 11308

Stohl, A., Forster, C., Frank, A., Seibert, P., and Wotawa, G.: Technical note: The Lagrangian particle dispersion model FLEXPART version 6.2, Atmos. Chem. Phys., 5, 2461–2474, doi:10.5194/acp-5-2461-2005, 2005. 11308

Stohl, A., Prata, A. J., Eckhardt, S., Clarisse, L., Durant, A., Henne, S., Kristiansen, N. I., Minikin, A., Schumann, U., Seibert, P., Stebel, K., Thomas, H. E., Thorsteinsson, T., Tørseth, K., and Weinzierl, B.: Determination of time- and height-resolved volcanic ash emissions and their use for quantitative ash dispersion modeling: the 2010 Eyjafjallajökull eruption, Atmos. Chem. Phys., 11, 4333–4351, doi:10.5194/acp-11-4333-2011, 2011. 11305, 11308, 11316, 11318, 11320, 11324

Timmreck, C.: Modeling the climatic effects of large explosive volcanic eruptions, in: Wiley Interdisciplinary Reviews: Climate Change, 3, 545–564, doi:10.1002/wcc.192, 2012. 11305

Wen, S. and Rose, W. I.: Retrieval of sizes and total masses of particles in volcanic clouds using AVHRR bands 4 and 5, J. Geophys. Res., 99, 5421–5431, 1994. 11305, 11310

Wind, G., da Silva, A. M., Norris, P. M., and Platnick, S.: Multi-sensor cloud retrieval simulator and remote sensing from model parameters – Part 1: Synthetic sensor radiance formulation, Geosci. Model Dev., 6, 2049–2062, doi:10.5194/gmd-6-2049-2013, 2013. 11306

Yu, T., Rose, W. I., and Prata, A. J.: Atmospheric correction for satellite-based volcanic ash mapping and retrievals using "split window" IR data from GOES and AVHRR, J. Geophys. Res., 107, AAC 10-1–AAC 10-19, doi:10.1029/2001JD000706, 2002. 11310

AMTD
7, 11303–11343, 2014

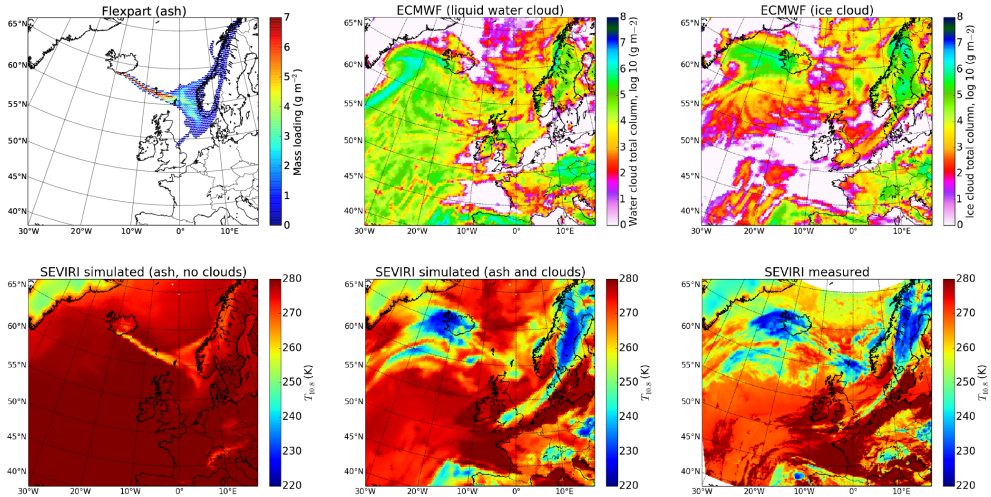

Figure 1. The total ash column as simulated by the Flexpart model (upper left). Only pixels with column density above 0.2 g m^{-2} are shown. The total liquid water (upper centre) and ice water (upper right) cloud columns from ECWMF analysis data. The simulated cloudless (lower left) and cloudy (lower centre) 10.8 µm brightness temperatures. (lower right) The measured brightness temperature of the 10.8 µm SEVIRI channel. All data shown are for 12:00 UTC, 15 April 2010.

AMTD
7, 11303–11343, 2014

Impact of meteorological clouds on detection of volcanic ash

A. Kylling et al.

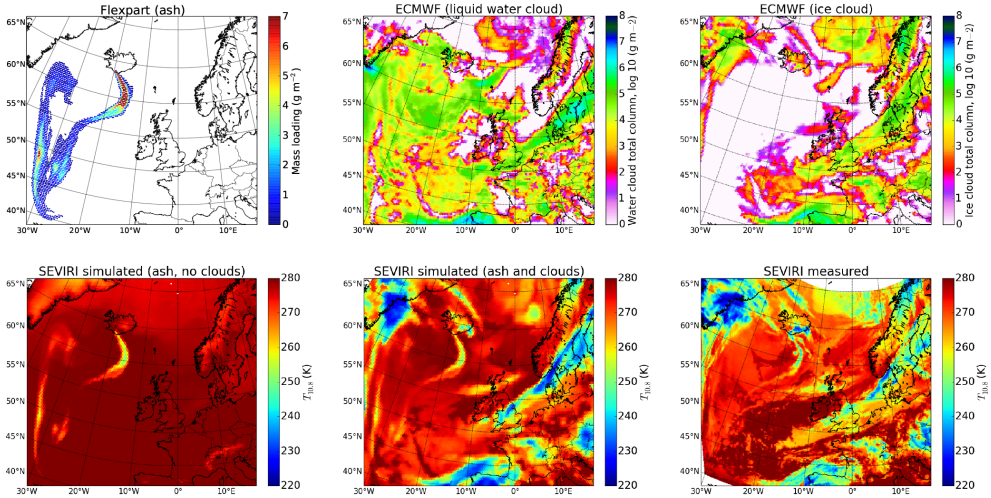

Figure 2. Same as Fig. 1, but for 18:00 UTC, 8 May 2010.

AMTD
7, 11303–11343, 2014

Impact of meteorological clouds on detection of volcanic ash

A. Kylling et al.

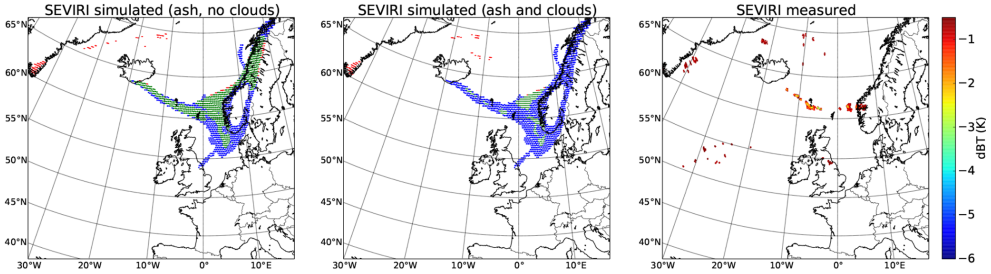

Figure 3. Ash detection: pixels flagged as ash by the reverse absorption technique in the cloudless simulation (left) and cloudy simulation (centre) compared to pixels with Flexpart ash columns above the low contamination limit ($0.2\,g\,m^{-2}$). The colour coding of the pixels are: co-incident (green): pixel identified as ash and contains ash in the Flexpart model simulation; false positive (red): pixel identified as ash, but does not contain ash; false negative (blue): pixel not flagged as ash, but contains ash. (Right) The $\Delta T = T_{10.8} - T_{12.0}$ brightness temperature difference calculated from SEVIRI measurements. Only data points with $\Delta T < -0.5\,K$ are shown. Data for 12:00 UTC, 15 April 2010.

AMTD
7, 11303–11343, 2014

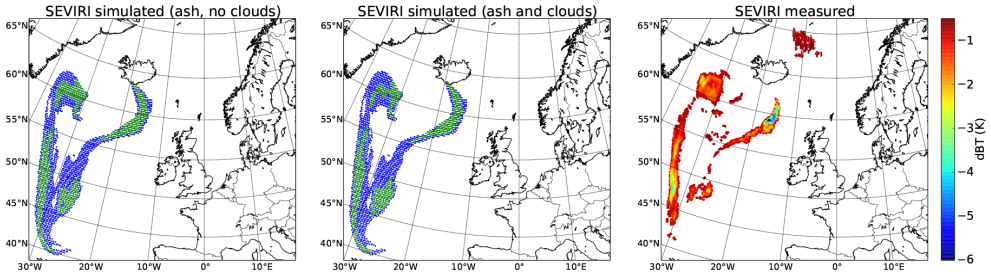

Figure 4. Same as Fig. 3, but for 18:00 UTC, 8 May 2010.

AMTD
7, 11303–11343, 2014

Impact of meteorological clouds on detection of volcanic ash

A. Kylling et al.

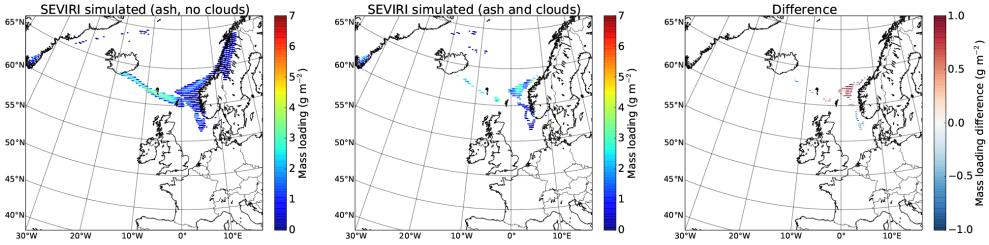

Figure 5. Ash retrieval: the ash mass loading retrieved from cloudless simulated SEVIRI images (left), and including meteorological clouds (middle). The difference between the ash mass loading retrieved from the cloudy and cloudless simulations (right). All data representative for 12:00 UTC, 15 April 2010.

AMTD
7, 11303–11343, 2014

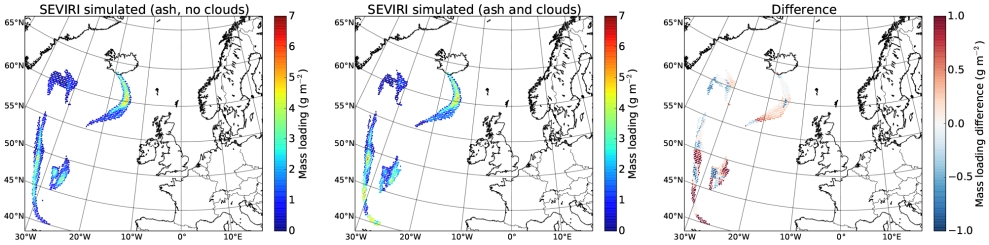

Figure 6. Same as Fig. 5, but data for 18:00 UTC, 8 May 2010.

AMTD
7, 11303–11343, 2014

Impact of meteorological clouds on detection of volcanic ash

A. Kylling et al.

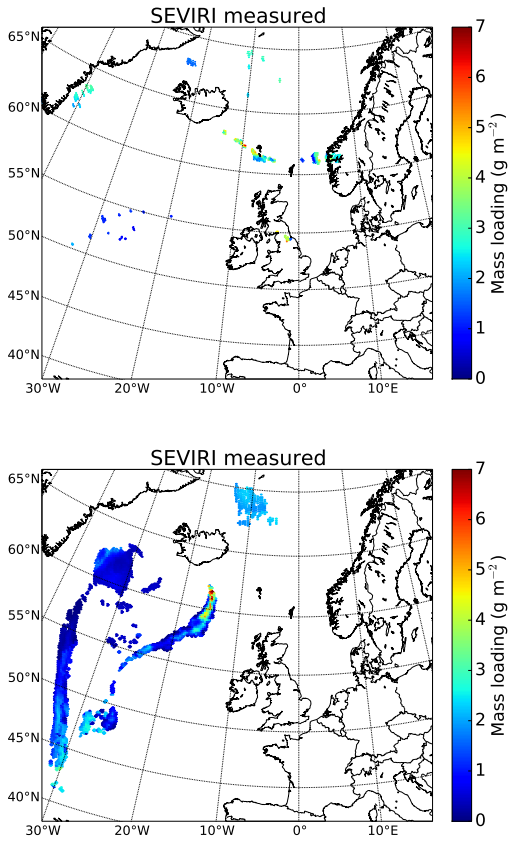

Figure 7. The ash mass loading retrieved from measured SEVIRI data for 12:00 UTC, 15 April 2010 (top) and 18:00 UTC, 8 May 2010 (bottom).

AMTD
7, 11303–11343, 2014

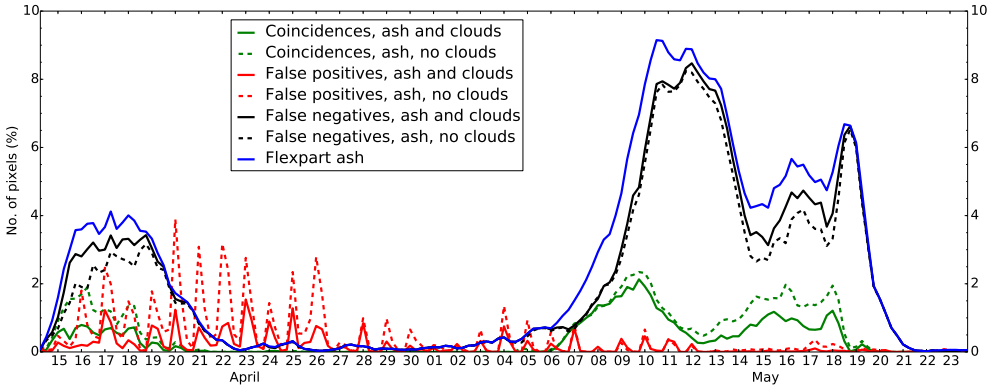

Figure 8. Ash detection time series for the Eyjafjallajökull 2010 eruption: the percentage of simulated pixels identified as ash (green lines). Dashed lines are for cloudless and solid lines for cloudy simulations. (Red lines) The percentage of false positive ash pixels with respect to the total number of pixels in the image. (Black lines) The percentage of false negative ash pixels with respect to the total number of pixels in the image. (Blue line, right *y* axis) The percentage of pixels with Flexpart ash mass loading above 0.2 g m^{-2}.

AMTD
7, 11303–11343, 2014

Impact of meteorological clouds on detection of volcanic ash

A. Kylling et al.

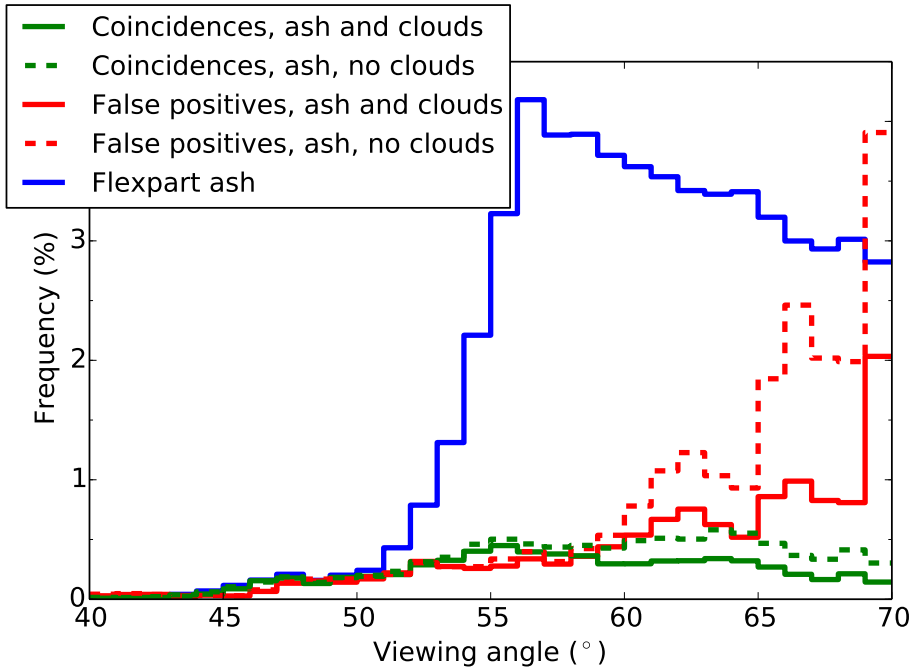

Figure 9. Ash detection as a function of viewing angle for the Eyjafjallajökull 2010 eruption: the frequency of pixels identified as ash in the Flexpart simulations (blue line), false positive pixels from ash detection (red line) and coincidences (green line). Solid (dashed) lines represent cloudy (cloudless) simulations.

AMTD
7, 11303–11343, 2014

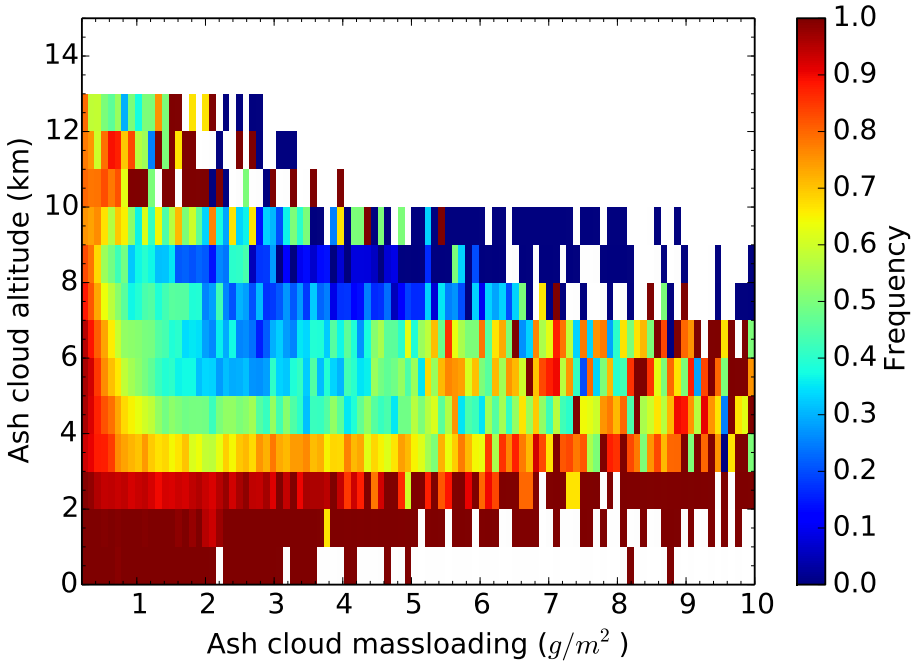

Figure 10. The relative frequency of false negatives (undetected ash pixels normalized to the number of Flexpart pixels) as a function of Flexpart ash mass loading and ash cloud altitude for the Eyjafjallajökull 2010 eruption. Results from cloudy simulation. Cloudless results are similar.

AMTD
7, 11303–11343, 2014

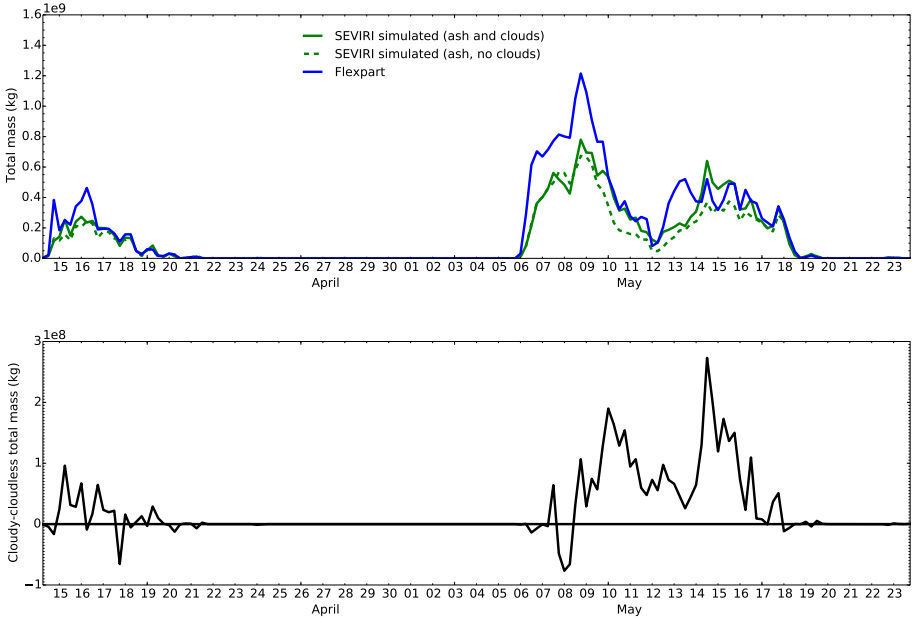

Figure 11. Ash retrieval time series for the Eyjafjallajökull 2010 eruption: total ash cloud mass from the Flexpart model (blue line) and as retrieved from simulated cloudless (green dashed line) and cloudy (green solid line) SEVIRI scenes (top). The difference between the cloudy and cloudless simulation from the above plot (bottom). Note that only coincident pixels are included in both plots.

AMTD
7, 11303–11343, 2014

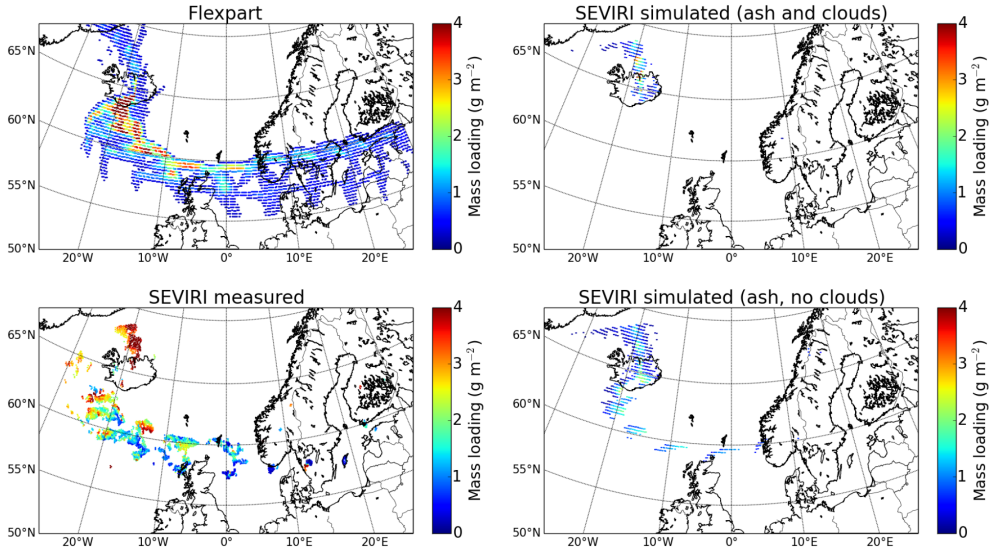

Figure 12. Modelled and retrieved ash mass loadings for the Grímsvötn 2011 eruption between 21–27 May 2011 shown as mosaics of six hourly fields. (Upper left) Flexpart model simulation, (lower left) retrieved from measured SEVIRI images, (upper right) retrieved from simulated cloudy SEVIRI images, (lower right) retrieved from simulated cloudless SEVIRI images. Note that composites of all individual 6 hourly scenes were constructed by taking for each pixel the maximum value of all scenes. For the measured SEVIRI data (lower left), all pixels with longitude > 10° W for the 22nd and 23rd, and for all subsequent days pixels with latitude > 63° N or longitude > 25° W or longitude > 30° E have been removed, as they are considered false positives.

AMTD
7, 11303–11343, 2014

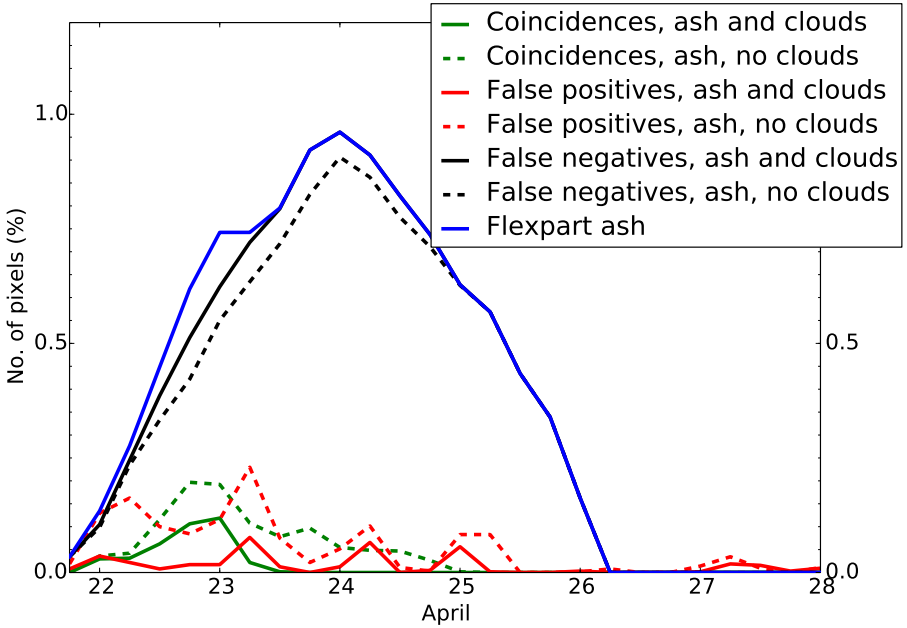

Figure 13. Similar to Fig. 8, but for the Grímsvötn 2011 eruption.

AMTD
7, 11303–11343, 2014

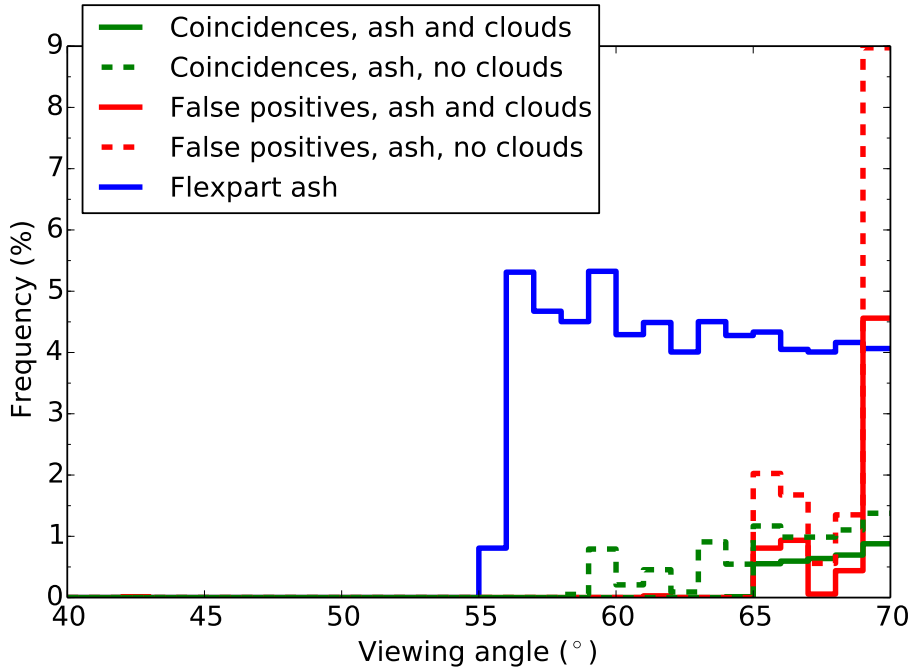

Figure 14. Similar to Fig. 9, but for the Grímsvötn 2011 eruption. The frequency of pixels identified as ash in the Flexpart simulations (blue line), false positive pixels from ash detection (red line) and coincidences (green line) are shown. Solid (dashed) lines represent cloudy (cloudless) simulations.

AMTD
7, 11303–11343, 2014

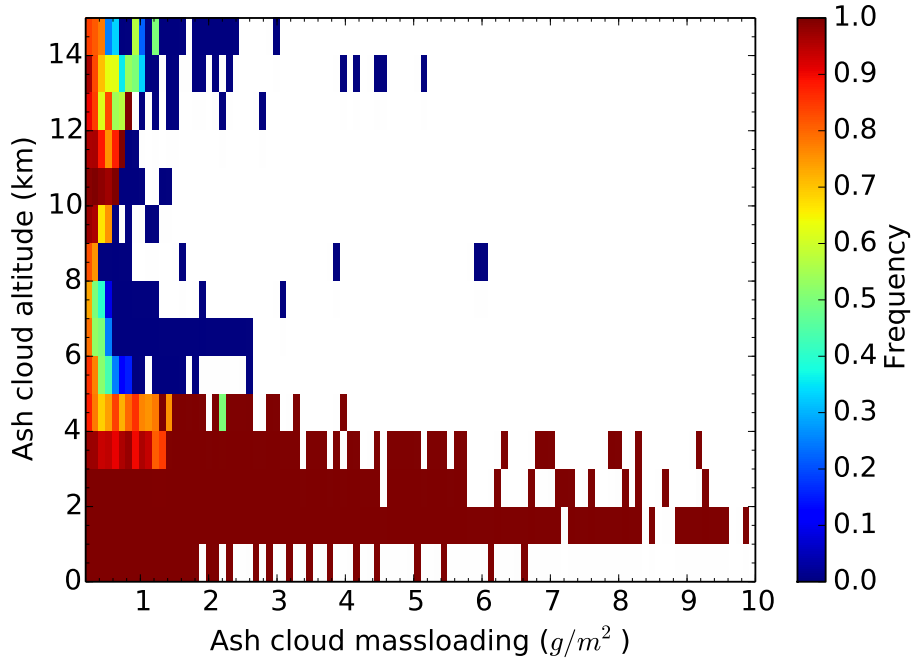

Figure 15. Similar to Fig. 10, but for the Grímsvötn 2011 eruption.

AMTD
7, 11303–11343, 2014

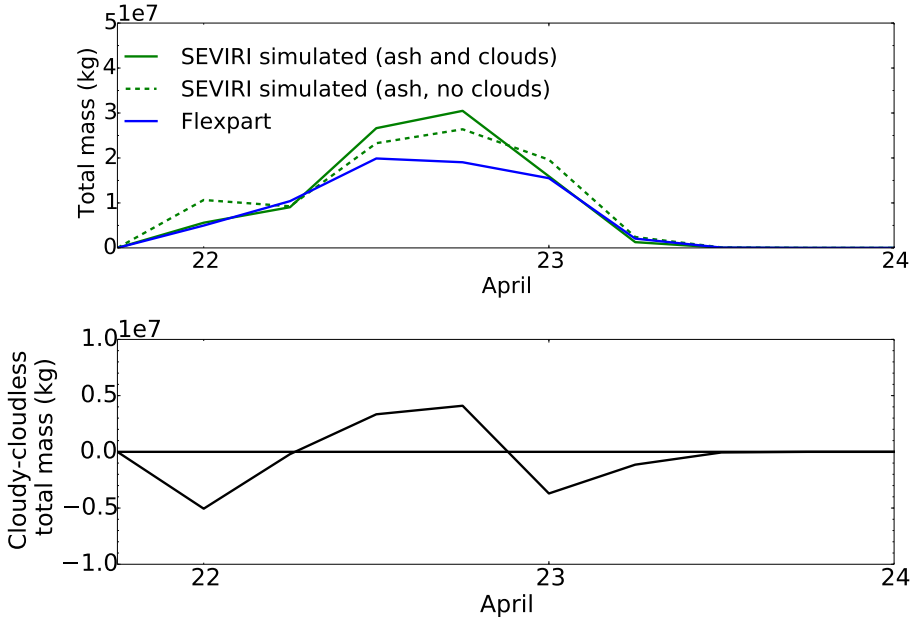

Figure 16. Similar to Fig. 11, but for the Grímsvötn 2011 eruption.

AMTD
7, 11303–11343, 2014